NASA Technical Paper 3417

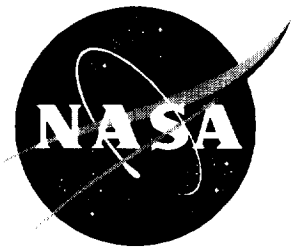

Local Performance Optimization for a Class of Redundant Eight-Degree-of-Freedom Manipulators

Robert L. Williams II
Langley Research Center • Hampton, Virginia

National Aeronautics and Space Administration
Langley Research Center • Hampton, Virginia 23681-0001

March 1994

Abstract

Local performance optimization for joint limit avoidance and manipulability maximization (singularity avoidance) is obtained by using the Jacobian matrix pseudoinverse and by projecting the gradient of an objective function into the Jacobian null space. Real-time redundancy optimization control is achieved for an eight-joint redundant manipulator having a three-axis spherical shoulder, a single elbow joint, and a four-axis spherical wrist. Symbolic solutions are used for both full-Jacobian and wrist-partitioned pseudoinverses, partitioned null-space projection matrices, and all objective function gradients. A kinematic limitation of this class of manipulators and the limitation's effect on redundancy resolution are discussed. Results obtained with graphical simulation are presented to demonstrate the effectiveness of local redundant manipulator performance optimization. Actual hardware experiments performed to verify the simulated results are also discussed. A major result is that the partitioned solution is desirable because of low computation requirements. The partitioned solution is suboptimal compared with the full solution because translational and rotational terms are optimized separately; however, the results show that the difference is not significant. Singularity analysis reveals that no algorithmic singularities exist for the partitioned solution. The partitioned and full solutions share the same physical manipulator singular conditions. When compared with the full solution, the partitioned solution is shown to be ill-conditioned in smaller neighborhoods of the shared singularities.

1. Introduction

Kinematically redundant manipulators, those with more degrees of freedom than task constraints, can have a secondary task of performance optimization in addition to the primary task of providing a Cartesian trajectory. Whitney (ref. 1) derived the pseudoinverse solution for the primary task in the framework of the resolved motion rate algorithm. Liegeois (ref. 2) suggested the local redundancy resolution method that is now commonly used. This method uses the Moore-Penrose pseudoinverse (ref. 3) to solve the primary task and projects the gradient of an objective function into the null space of the Jacobian matrix to solve the secondary task. A good review of pseudoinverse-based local redundancy resolution is given in references 4 and 5.

Many authors who claim that the Liegeois method is too slow for real-time application to three-dimensional redundant manipulators have developed alternate methods that focus on reducing the computational requirements (e.g., refs. 6–8). The approach described in this paper applies the Liegeois method in real time by using symbolical pseudoinverses for both full and partitioned Jacobian matrices.

Other authors have investigated the use of partitioned or symbolic methods in redundancy resolution. Kirćanski and Petrović (ref. 9) decompose a manipulator into redundant and nonredundant subassemblies; the redundant joints are solved by singular value decomposition or equivalent methods, and the nonredundant joints are solved analytically. Holt (ref. 10) presents numerical computation of the approximate pseudoinverse for a six-axis manipulator near singularities by taking advantage of the wrist partitioning of the Jacobian matrix. Chevallereau and Khalil (ref. 11) present symbolic pseudoinverse calculations for nonredundant manipulators at singularities and for a six-degree-of-freedom manipulator on a linear track. In reference 12, Podhorodeski, Goldenberg, and Fenton use screw theory in an orthogonal decomposition of a Jacobian matrix for a redundant manipulator to determine analytical expressions for the particular solution and the null-space basis.

The references in the previous paragraph are limited in scope in that they deal either with nonredundant manipulators at singularities or with redundant manipulators having only one degree of redundancy. In the partitioned solution of reference 9, only three joints are treated as redundant; this treatment is limiting because the remaining four joints do not participate in optimization. This paper develops both full and wrist-partitioned solutions for

a manipulator with two redundant degrees of freedom. Here the partitioned solution is more useful because each subassembly has a redundant degree of freedom; thus, performance optimization is accomplished for each. To the author's knowledge, this work has not been published before. The motivation for this work is real-time redundancy resolution of manipulators for remote space applications; Earth-based applications can benefit also. This work was performed with graphical simulation and actual hardware.

This paper describes real-time local performance optimization efforts for an eight-joint redundant manipulator having a three-axis spherical shoulder S, a single elbow joint E, and a four-axis spherical wrist W. (See fig. 1.) The Advanced Research Manipulator II (ARMII) is an eight-axis manipulator in this class. NASA Langley Research Center has two of these arms. This paper has four objectives: (1) To apply the Liegeois method for local performance optimization (joint limit avoidance and manipulability maximization) of the eight-axis manipulator in figure 1 and implement the method on actual hardware in real time. (2) To investigate a kinematic limitation of this class of manipulators and report its effect on redundancy resolution. (3) To present closed-form symbolic solutions for reduced computation. (4) To develop a wrist-partitioned solution for reduced computation and show that it is as valid, robust, and effective as the full solution.

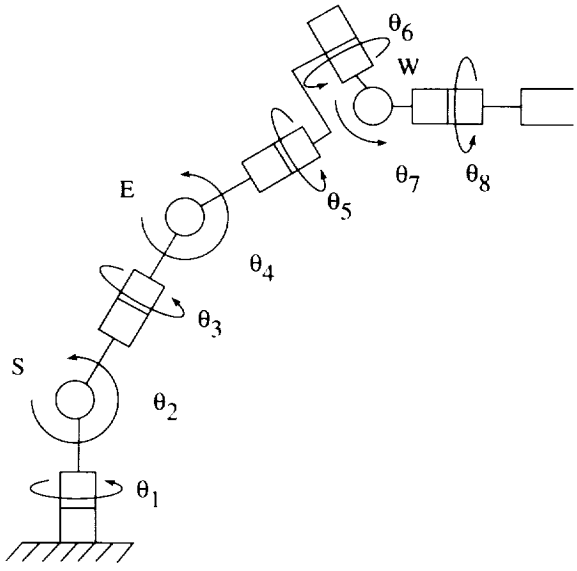

Figure 1. Class of eight-axis manipulators.

This paper is organized as follows. Local performance optimization of redundant manipulators is presented for general applications and for the configuration of figure 1. A partitioned solution is developed where optimization is accomplished for each subassembly. Singularity analysis is presented for both full and partitioned solutions. Results are presented to show the effectiveness of local performance optimization. Results are also given to compare the effectiveness of the partitioned and full solutions. A kinematic limitation of this manipulator is investigated, the limitation's effect on redundancy resolution is described, and proposed design alternatives are presented to alleviate the problems. Finally, the accomplishments of this paper are summarized.

2. Symbols

a_{i-1}	Denavit-Hartenberg parameter
c_i	$\cos\theta_i$
d_i	Denavit-Hartenberg parameter
d_3, d_5	Denavit-Hartenberg parameters, fixed manipulator lengths
H	objective function for optimization
$\nabla\mathbf{H}$	gradient of H
$\nabla\mathbf{H}_{i\neq4}$	$\nabla\mathbf{H}$ excluding the fourth term
H_A	objective function for arm subassembly optimization
$\nabla\mathbf{H}_{A,i\neq4}$	gradient of H_A excluding the fourth term
H_J	objective function for joint limit avoidance
H_M	objective function for manipulability maximization
H_W	objective function for wrist subassembly optimization
$\nabla\mathbf{H}_W$	gradient of H_W
$\mathbf{I}_p$	identity matrix of order p
$\mathbf{J}$	manipulator Jacobian matrix
$\mathbf{J}^*$	Moore-Penrose pseudoinverse of Jacobian matrix
$\mathbf{J}_4$	column 4 of $\mathbf{J}$ with row 1 removed
$\mathbf{J}_{5\times7}$	reduced Jacobian matrix with row 1 and column 4 removed, dimension 5×7
$\mathbf{J}^*_{5\times7}$	Moore-Penrose pseudoinverse of reduced Jacobian matrix, dimension 7×5
$\mathbf{J}_{UL}$	upper left partition of $\mathbf{J}$, order 3×4

$\mathbf{J}_{LL}$	lower left partition of $\mathbf{J}$, order 3×4
$\mathbf{J}_{LR}$	lower right partition of $\mathbf{J}$, order 3×4
$\mathbf{J}_{UL4}$	column 4 of $\mathbf{J}_{UL}$ with row 1 removed
$\mathbf{J}^*_{1UL4}$	Moore-Penrose pseudoinverse of $\mathbf{J}_{UL}$ with row 1 and column 4 removed
$\mathbf{J}^*_{LR}$	Moore-Penrose pseudoinverse of $\mathbf{J}_{LR}$
k	scalar gain for homogeneous solution
k_A	scalar gain for arm subassembly homogeneous solution
k_J	scalar gain for joint limit avoidance homogeneous solution
k_M	scalar gain for manipulability maximization homogeneous solution
k_W	scalar gain for wrist subassembly homogeneous solution
m	dimension of task space
n	dimension of joint space
${}^4_8\mathbf{R}$	rotation matrix representing orientation of frame {8} in frame {4}
$\Re^{i \times j}$	array of real numbers, dimension $i \times j$
s_i	$\sin \theta_i$
$\mathbf{v}$	translational terms of $\dot{\mathbf{X}}$, $\{ \dot{x} \quad \dot{y} \quad \dot{z} \}^T$
$\mathbf{v}_i$	$\mathbf{v}$ with first term removed
$\dot{\mathbf{X}}$	Cartesian translational and rotational end-effector velocity
$\dot{\mathbf{X}}_1$	$\dot{\mathbf{X}}$ with first term removed
α_{i-1}	Denavit-Hartenberg parameter
θ_{ci}	center of travel for joint i
θ_i	Denavit-Hartenberg parameter, joint angle i
$\Delta\theta_i$	half range of travel for joint i
$\boldsymbol{\theta}$	vector of eight joint angles
$\dot{\boldsymbol{\theta}}$	joint rate vector
$\dot{\boldsymbol{\theta}}_A$	arm subassembly joint rates, $\{ \dot{\theta}_1 \quad \dot{\theta}_2 \quad \dot{\theta}_3 \quad \dot{\theta}_4 \}^T$
$\dot{\boldsymbol{\theta}}_{AH,i\neq4}$	homogeneous solution for arm subassembly joint rates excluding joint 4
$\dot{\boldsymbol{\theta}}_{AP,i\neq4}$	particular solution for arm subassembly joint rates excluding joint 4
$\dot{\boldsymbol{\theta}}_{AT}$	total solution for arm subassembly joint rates
$\dot{\boldsymbol{\theta}}_{AT,i\neq4}$	total solution for arm subassembly joint rates excluding joint 4
$\dot{\boldsymbol{\theta}}_{H,i\neq4}$	homogeneous solution for joint rates excluding joint 4
$\dot{\boldsymbol{\theta}}_i$	ith joint rate
$\dot{\boldsymbol{\theta}}_{P,i\neq4}$	particular solution for joint rates excluding joint 4
$\dot{\boldsymbol{\theta}}_{T,i\neq4}$	total solution for joint rates excluding joint 4
$\dot{\boldsymbol{\theta}}_W$	wrist subassembly joint rates, $\{ \dot{\theta}_5 \quad \dot{\theta}_6 \quad \dot{\theta}_7 \quad \dot{\theta}_8 \}^T$
$\dot{\boldsymbol{\theta}}_{WH}$	homogeneous solution for wrist subassembly joint rates
$\dot{\boldsymbol{\theta}}_{WP}$	particular solution for wrist subassembly joint rates
$\dot{\boldsymbol{\theta}}_{WT}$	total solution for wrist subassembly joint rates
$\boldsymbol{\omega}$	rotational terms of $\dot{\mathbf{X}}$, $\{ \omega_x \quad \omega_y \quad \omega_z \}^T$

Mathematical notation:

$\{ \}$	Cartesian coordinate frame
$\{., ., \ldots, .\}^T$	vector components
$\lvert \ \rvert$	determinant of a matrix

Arm reference points:

E	elbow
EE	end effector
S	shoulder
W	wrist

Coordinate frames:

4	elbow
8	wrist

Abbreviations:

ARMII	Advanced Research Manipulator II
JLA	joint limit avoidance
MM	manipulability maximization

3. Local Performance Optimization Using Redundancy

3.1. General Redundant Solution

The resolved motion rate algorithm (ref. 1) is a common method for Cartesian control of redundant manipulators. Joint rates $\dot{\boldsymbol{\theta}}$ are mapped to end-effector Cartesian velocities $\dot{\mathbf{X}}$ by the Jacobian matrix $\mathbf{J}$ as follows:

$$\dot{\mathbf{X}} = \mathbf{J}\dot{\boldsymbol{\theta}} \tag{1}$$

In equation (1), $\dot{\mathbf{X}} \in \Re^{m\times 1}$, $\mathbf{J} \in \Re^{m\times n}$, and $\dot{\boldsymbol{\theta}} \in \Re^{n\times 1}$, where m is the dimension of the task space ($m = 6$ for spatial Cartesian control) and n is the dimension of the joint space ($n = 8$ in this paper). To command a trajectory $\dot{\mathbf{X}}$ to a manipulator, $\dot{\boldsymbol{\theta}}$ must be solved.

A kinematically redundant manipulator has more degrees of freedom than required to perform the task; that is, $m < n$. In this case, equation (1) is underconstrained, and an infinite number of solutions for $\dot{\boldsymbol{\theta}}$ generally exist. A resolved motion rate solution (ref. 2) is expressed as follows:

$$\dot{\boldsymbol{\theta}} = \mathbf{J}^*\dot{\mathbf{X}} + k(\mathbf{I}_n - \mathbf{J}^*\mathbf{J})\nabla\mathbf{H} \tag{2}$$

The first term of equation (2) is the particular solution. The matrix $\mathbf{J}^*$ is the Moore-Penrose pseudoinverse (ref. 3) of the Jacobian matrix, which provides the least-squares solution of equation (1) to achieve the Cartesian velocity command (called the primary task). The second term, the homogeneous solution, causes zero motion of the end effector. The linear operator $(\mathbf{I}_n - \mathbf{J}^*\mathbf{J})$ projects an arbitrary vector into the null space of the Jacobian matrix. This null-space projection matrix provides the self-motion of the redundant manipulator. To optimize performance criteria, the gradient of an objective function of joint angles $\nabla\mathbf{H}$ is used (ref. 2). The gain k is positive to maximize H and negative to minimize H.

Figure 2 shows a geometric interpretation of the Jacobian matrix null space for the manipulator in figure 1. The self-motion of this manipulator is the orbit of the elbow joint about the line SW. That is, by a reconfiguration of joints, the position and orientation of the end effector can be held fixed while the elbow joint assumes any position along the circle of figure 2.

3.2. Eight-Axis Redundant Solution

This section presents the adaptation of the general solution in equation (2) to the eight-axis manipulator shown in figure 1. To the author's knowledge, the solutions in this section have not been published before. This manipulator can be viewed as two subassemblies: an arm portion (θ_1, θ_2, θ_3, θ_4) responsible primarily for positioning and a spherical wrist (θ_5, θ_6, θ_7, θ_8) centered at W responsible primarily for orienting the end effector. The arm subassembly consists of a three-axis spherical shoulder centered at S, and a single elbow joint at E. The four-axis wrist mechanism is a roll-yaw-pitch-roll mechanism.

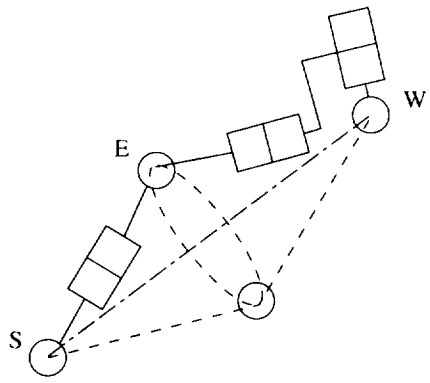

Figure 2. Geometric interpretation of eight-axis arm self-motion.

The ARMII is an eight-axis manipulator of the class shown in figure 1. The theory of this paper has been implemented in real-time (33 Hz update) on the ARMII. Appendix A presents the following information for the ARMII: a photograph, the design attributes, the kinematic diagram, the Denavit-Hartenberg parameters, the joint limits, the Jacobian matrix referred to frame {4} (which is symbolically the least complex among all possibilities), and a velocity coordinate transformation for use with this Jacobian matrix. In addition, reference 13 presents ARMII forward and inverse position and velocity kinematics equations, where the inverse solutions are limited to six degrees of freedom.

3.2.1. Independent solution for elbow joint rate. For manipulators with a spherical wrist, a spherical shoulder, and a single elbow joint, the length of reach from S to W is a function of only the elbow joint angle. The SEW manipulator subassembly is shown in figure 3. To simplify the resolved rate solution, the elbow joint rate is calculated independently of the remaining unknown joint rates. For the eight-axis arm, this solution (ref. 13) is given as follows:

$$\dot{\theta}_4 = \frac{-1}{d_5}\left(\dot{x} + \frac{d_3c_4 + d_5}{d_3s_4}\dot{y}\right) \tag{3}$$

In equation (3), d_3 and d_5 are kinematic parameters (fig. 3), $\dot{x}$ and $\dot{y}$ are wrist Cartesian velocity commands expressed in frame {4}, and s_4 and c_4 are the sine and cosine of the elbow joint angle θ_4. Equation (3) is the general form of the particular solution for the elbow rate because the required wrist velocities can be calculated from commanded velocities in frames different from the wrist (but rigidly attached to frame {8}) via rigid-body velocity transformations. (See ref. 14.)

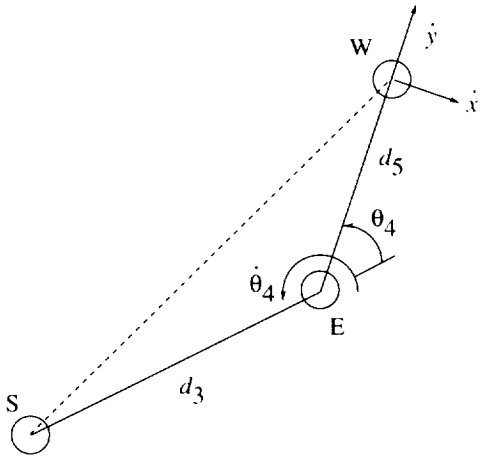

Figure 3. Elbow joint geometry.

*3.2.2. **Reduced Jacobian solution.*** Given the solution in equation (3), the fourth column of the Jacobian matrix multiplied by $\dot{\boldsymbol{\theta}}_4$ is moved to the left side of equation (1). The result is a 6×7 Jacobian matrix that has a maximum rank of 5 because the elbow relationship uses one degree of freedom. Therefore, either row 1 or 2 must be removed from both sides of equation (1); row 1 is removed because it has more symbolic terms. (See appendix A.) With this reduced Jacobian matrix, the particular solution for the remaining joint rates is

$$\dot{\boldsymbol{\theta}}_{P,i\neq 4} = \mathbf{J}^*_{5\times 7}\left(\dot{\mathbf{X}}_1 - \mathbf{J}_4\dot{\boldsymbol{\theta}}_4\right) \tag{4a}$$

The vector $\dot{\mathbf{X}}_1$ is the Cartesian velocity command and $\mathbf{J}_4$ is the fourth column of the Jacobian matrix; both have row 1 removed. The pseudoinverse of the reduced Jacobian matrix ($\mathbf{J}^*_{5\times 7}$) was derived with a computer symbolic manipulation program (ref. 15) with $\mathbf{J}^* = \mathbf{J}^T(\mathbf{J}\mathbf{J}^T)^{-1}$. When $\mathbf{J}\mathbf{J}^T$ is singular, a numerical singular value decomposition can be used to calculate $\mathbf{J}^*_{5\times 7}$; the exact Cartesian trajectory cannot be achieved, but this alternate solution is the best available given the singular condition.

No loss of generality occurs when equations (3) and (4a) are used for the particular solution to equation (1). If the geometric relationship of equation (3) is not exploited for the solution of $\dot{\boldsymbol{\theta}}_4$, the pseudoinverse of the 6×8 Jacobian matrix and equation (3) always yield the same value.

The homogeneous solution of equation (1) for local redundancy optimization is

$$\dot{\boldsymbol{\theta}}_{H,i\neq 4} = k(\mathbf{I}_7 - \mathbf{J}^*_{5\times 7}\mathbf{J}_{5\times 7})\nabla\mathbf{H}_{i\neq 4} \tag{4b}$$

The null-space projection operator is a square matrix of order 7 that was obtained from the reduced Jacobian matrix. The homogeneous term for $\dot{\boldsymbol{\theta}}_4$ is zero because of the geometric elbow constraint. Any addition to the particular solution (eq. (3)) would cause a deviation from the commanded trajectory. The fourth term of the constraint function gradient is excluded, as explained in the next paragraph.

Again, no loss of generality is incurred when equation (4b) is used as the homogeneous solution to equation (1). In general, $\mathbf{J}\mathbf{J}^* = \mathbf{I}_m$, but $\mathbf{J}^*\mathbf{J} \neq \mathbf{I}_n$. However, because of the geometric elbow constraint of the eight-axis arm, the fourth row and column of $\mathbf{J}^*\mathbf{J}$ are the same as the fourth row and column of the identity matrix, when $\mathbf{J}$ is the full 6×8 Jacobian matrix. The null-space projection matrix thus has zeros for the fourth row and column. This condition has two consequences. (1) Because the fourth row is zero, a homogeneous term for $\dot{\boldsymbol{\theta}}_4$ does not exist. (2) Because the fourth column is zero, the partial derivative of a constraint function with respect to θ_4 never adds to the homogeneous terms for the other joint rates.

The total solution to equation (1) is as follows. The particular solution for the elbow joint rate is given in equation (3), and the total solution for the remaining joints is the sum of the particular and homogeneous solutions:

$$\dot{\boldsymbol{\theta}}_{T,i\neq 4} = \dot{\boldsymbol{\theta}}_{P,i\neq 4} + \dot{\boldsymbol{\theta}}_{H,i\neq 4} \tag{4c}$$

*3.2.3. **Partitioned reduced Jacobian solution.*** To greatly reduce the computation requirement, a partitioned approach for the particular solution of equation (1) was implemented. The particular solution for the full Jacobian matrix requires 25 times more computation time than the partitioned particular solution (ref. 15). This section discusses the partitioned solution and extends the theory to include the partitioned homogeneous solution.

Wrist partitioning is a common method for solving the inverse position and velocity problems of

nonredundant industrial manipulators with spherical wrists. For nonredundant manipulators, the full and partitioned solutions yield the same results. However, for redundant manipulators, the partitioned solution yields a suboptimal result because the constraints are optimized separately for translation and orientation. For instance, the full particular solution for joint rates is the least-squares solution. The magnitude of the partitioned solution joint rates is higher, but the difference is not significant. (See section 4.2.1.)

For a manipulator with a spherical wrist, equation (1) can be written in the following partitioned form:

$$\begin{Bmatrix} \mathbf{v} \\ \boldsymbol{\omega} \end{Bmatrix} = \begin{bmatrix} \mathbf{J}_{UL} & 0 \\ \mathbf{J}_{LL} & \mathbf{J}_{LR} \end{bmatrix} \begin{Bmatrix} \dot{\boldsymbol{\theta}}_A \\ \dot{\boldsymbol{\theta}}_W \end{Bmatrix} \tag{5}$$

The vectors $\mathbf{v}$ and $\boldsymbol{\omega}$ are the translational and rotational Cartesian velocity commands. The Jacobian matrix is partitioned into upper-left, lower-left, and lower-right 3×4 submatrices. The vector $\dot{\boldsymbol{\theta}}_A$ represents the translational (arm) joint rates 1 through 4, and $\dot{\boldsymbol{\theta}}_W$ the rotational (wrist) joint rates 5 through 8. The upper-right submatrix in equation (5) is the 3×4 zero matrix because of the spherical wrist: The wrist joint rates do not affect the translational velocities of the wrist center. In the translational equations, $\dot{\theta}_4$ is first determined from equation (3). The particular solution for the remaining arm joint rates is as follows:

$$\dot{\boldsymbol{\theta}}_{AP,i\neq 4} = \mathbf{J}^*_{1UL4}\left(\mathbf{v}_1 - \mathbf{J}_{UL4}\dot{\theta}_4\right) \tag{6a}$$

The joint rate vector $\dot{\boldsymbol{\theta}}_{AP,i\neq 4}$ contains the translational joint rates excluding $\dot{\theta}_4$, $\mathbf{J}^*_{1UL4}$ is the 3×2 pseudoinverse of $\mathbf{J}_{UL}$ with column 4 and row 1 removed, $\mathbf{v}_1$ is $\mathbf{v}$ with row 1 removed, and $\mathbf{J}_{UL4}$ is column 4 of $\mathbf{J}_{UL}$ with row 1 removed.

The homogeneous solution for the arm joint rates excluding $\dot{\theta}_4$ is given in the following equation, where H_A is a function of the arm joint angles:

$$\dot{\boldsymbol{\theta}}_{AH,i\neq 4} = k_A(\mathbf{I}_3 - \mathbf{J}^*_{1UL4}\mathbf{J}_{1UL4})\nabla \mathbf{H}_{A,i\neq 4} \tag{6b}$$

The total arm joint rate solution is as follows. The particular solution for the elbow joint rate is given in equation (3). Again, the homogeneous solution for $\dot{\theta}_4$ is zero. The total solution for the remaining arm joints is the sum of the particular and homogeneous solutions:

$$\dot{\boldsymbol{\theta}}_{AT,i\neq 4} = \dot{\boldsymbol{\theta}}_{AP,i\neq 4} + \dot{\boldsymbol{\theta}}_{AH,i\neq 4} \tag{6c}$$

For the same reasons stated for the nonpartitioned solution, no loss of generality is incurred by using equation (3) and reducing $\mathbf{J}_{UL}$ to $\mathbf{J}_{1UL4}$ for both particular and homogeneous translational solutions.

The particular and homogeneous wrist joint rate solutions are given in equations (7a) and (7b). The total wrist joint rate solution is the sum of the particular and homogeneous solutions:

$$\dot{\boldsymbol{\theta}}_{WP} = \mathbf{J}^*_{LR}\left(\boldsymbol{\omega} - \mathbf{J}_{LL}\dot{\boldsymbol{\theta}}_{AT}\right) \tag{7a}$$

$$\dot{\boldsymbol{\theta}}_{WH} = k_W(\mathbf{I}_4 - \mathbf{J}^*_{LR}\mathbf{J}_{LR})\nabla \mathbf{H}_W \tag{7b}$$

$$\dot{\boldsymbol{\theta}}_{WT} = \dot{\boldsymbol{\theta}}_{WP} + \dot{\boldsymbol{\theta}}_{WH} \tag{7c}$$

The full $\mathbf{J}_{LR}$ is used for the rotational equations so the order of the pseudoinverse $\mathbf{J}^*_{LR}$ is 4×3. The effect of the total arm joint solution must be subtracted for the wrist particular solution. The objective function H_W is a function of the wrist joint angles.

Symbolic expressions for $\mathbf{J}^*_{1UL4}$ and $\mathbf{J}^*_{LR}$ are given in appendix B. Also, the symbolic forms of the partitioned null-space projection matrices are given in appendix C.

3.2.4. Eight-axis arm singularity analysis. Singularity conditions for redundant manipulators arise when $|\mathbf{J}\mathbf{J}^T| = 0$. This matrix is symmetric and positive semidefinite ($|\mathbf{J}\mathbf{J}^T| \geq 0$). For the partitioned solution, singularity analysis is presented as follows. The calculation of $\dot{\theta}_4$ in equation (3) fails when $d_3 = 0$ or $d_5 = 0$ (neither is possible) or when $\theta_4 = 0°, 180°$. The joint angles follow Craig's convention (ref. 14), and the zero position for all joint angles is given in figure A2 of appendix A. The singularity condition for the remaining translational joints is independent of θ_1. (In appendix B, D_{UL} is given.)

$$\left|\mathbf{J}_{1UL4}\mathbf{J}^T_{1UL4}\right| = d_3^2 s_4^2 D_{UL} = 0 \tag{8}$$

Of the three terms in equation (8), only the last two can become zero. When $\theta_4 = 0°, 180°$, the translational joints are in the elbow work space limit singularity. At $\theta_4 = 0°$, the elbow is fully extended and the freedom to translate along EW has been instantaneously lost. Similarly at $\theta_4 = 180°$, the elbow is folded upon itself. The term D_{UL} can become zero in two ways.

1. $\theta_2 = 0°, 180°$ and $\theta_3 = \pm 90°$. (See fig. 4(a).) In this case, joint 4 can instantaneously move W tangentially to the link EW, and joint 1, 2,

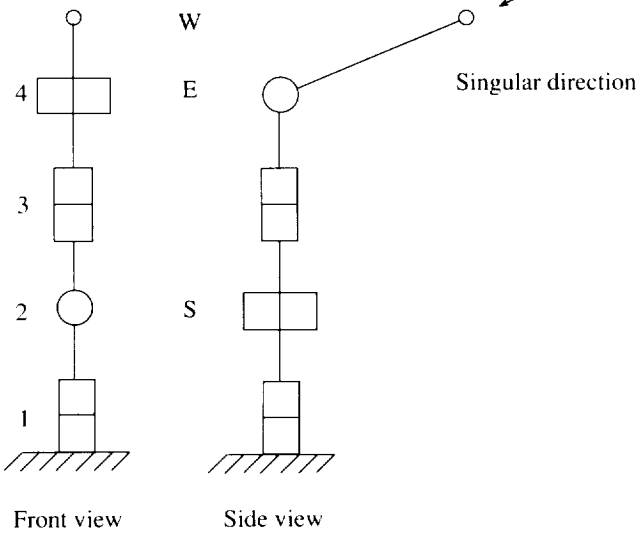

(a) Internal singularity for arm subassembly.

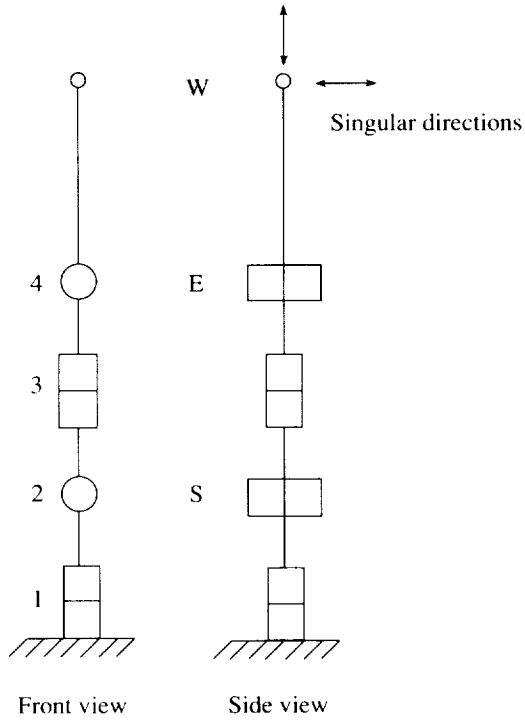

(b) Doubly degenerate singularity for arm subassembly.

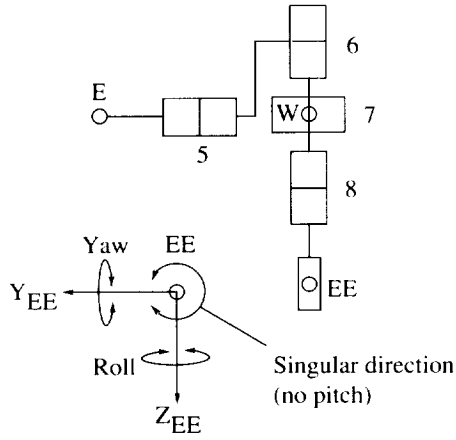

(c) Internal singularity for wrist subassembly.

Figure 4. Singularity configurations.

or 3 can move W perpendicular to the plane of the side view. However, the freedom to translate radially along link EW is gone (singular direction).

2. $\theta_2 = \theta_4 = 0°, 180°$. This case is doubly degenerate with respect to translation. (See fig. 4(b).) The zeros of D_{UL} were obtained numerically because of its complexity.

The singularity condition for the wrist joints is independent of θ_5 and θ_8 and is given as follows:

$$\left|\mathbf{J}_{LR}\mathbf{J}_{LR}^T\right| = 2\left(1 - s_6^2 s_7^2\right) = 0 \qquad (9)$$

The wrist singularity occurs only when $\theta_6 = \pm 90°$ and $\theta_7 = \pm 90°$ simultaneously. As shown in figure 4(c), joints 5 and 7 provide yaw, joints 6 and 8 provide roll, but the freedom to pitch has been lost.

The symbol EE in figure 4(c) represents the end effector.

Table 1 summarizes the four singularity conditions for the general eight-axis arm. For the ARMII, as shown in table A2, the cases where θ_2 or θ_4 equal 180° and $\theta_7 = +90°$ are out of joint motion ranges, and the case $\theta_6 = \pm 90°$ coincides with the joint limits.

Table 1. Singularity Conditions

Number	Condition
1	$\theta_4 = 0°, 180°$
2	$\theta_2 = 0°, 180°$; $\theta_3 = \pm 90°$
3	$\theta_2 = \theta_4 = 0°, 180°$
4	$\theta_6 = \pm 90°$; $\theta_7 = \pm 90°$

Entries 1 and 3 (3 is a subset of 1) are work space limit singularities, and entries 2 and 4 are work space interior singularities. These singularity conditions were derived from the partitioned solution. The symbolic analysis for $|\mathbf{J}_{5\times7}\mathbf{J}_{5\times7}^T|$ is too complicated for analytical treatment. With the exception of the elbow joint work space limit singularity, $\theta_4 = 0°, 180°$. However, an intensive numerical computer search indicated that the full Jacobian matrix shares all four singularity conditions from table 1. The computer search also indicated that no additional singularities exist for the full solution. This result is expected because of the spherical wrist. Reference 16 shows that for a nonredundant manipulator with a spherical wrist, the partitioned arm and wrist singularities correspond one-to-one with the singularities of the full Jacobian matrix. This condition is not true for manipulators with a nonspherical wrist. The computer search involved all possible combinations of joint angles in steps of 5° over a full 360° rotation. At each step, $|\mathbf{J}_{5\times7}\mathbf{J}_{5\times7}^T|$ was computed and the cases near zero were printed.

In the neighborhood of manipulator singularities, both full and partitioned symbolic solutions become ill-conditioned. A numerical singular value decomposition solution can be used, where the trajectory cannot be satisfied, but the alternate solution is the best available given the singular condition.

3.3. Objective Functions

This section presents three objective functions for use in the homogeneous solutions to optimize the performance of a redundant manipulator. Two objective functions have been implemented for the full and partitioned solutions: joint limit avoidance and manipulability maximization (singularity avoidance). A third objective function for obstacle avoidance is discussed but has not been used.

The following function was proposed by Liegeois (ref. 2) to allow the manipulator to avoid joint limits:

$$H_J(\boldsymbol{\theta}) = \sum_{i=1}^{n} \left(\frac{\theta_i - \theta_{ci}}{\Delta\theta_i} \right)^2 \tag{10}$$

where θ_i is the current value for joint i, θ_{ci} is the center of travel for joint i, and $\Delta\theta_i$ is half the range of travel for joint i. The function is normalized by its denominator so that each joint has equal weight regardless of its range of travel. This function is minimized for joint limit avoidance. Equation (10) is defined for the full solution. For the partitioned solution, H_A is defined for $i = 1$ to 4, and H_W for $i = 5$ to 8. Klein and Huang (ref. 5) state that equation (10) leads to a suboptimal joint limit avoidance solution. The optimal norm to use is the maximum norm; they use the p-norm to approach the maximum norm with a tractable gradient. Equation (10) is used in this paper.

From reference 17 Yoshikawa's definition of manipulability is as follows:

$$H_M(\boldsymbol{\theta}) = \sqrt{\left|\mathbf{J}\mathbf{J}^T\right|} \tag{11}$$

This function is maximized to ensure that the manipulator operates far from singular configurations. The value of equation (11) is zero when the manipulator is in a singular configuration. For the full homogeneous solution, the function is $H_M = \sqrt{|\mathbf{J}_{5\times7}\mathbf{J}_{5\times7}^T}$ and for the partitioned solution the functions are $H_A = \sqrt{|\mathbf{J}_{1UL4}\mathbf{J}_{1UL4}^T|}$ and $H_W = \sqrt{|\mathbf{J}_{LR}\mathbf{J}_{LR}^T|}$. The gradients of the two implemented objective functions have been derived symbolically.

Yoshikawa (ref. 17) proposes minimization of the following function for obstacle avoidance:

$$H_o(\boldsymbol{\theta}) = \frac{1}{2}(\boldsymbol{\theta} - \theta_r)^T \mathbf{W} (\boldsymbol{\theta} - \theta_r) \tag{12}$$

where θ_r is a single constant manipulator configuration that is good for avoiding collisions with an obstacle, and $\mathbf{W}$ is a diagonal matrix with positive gains. Except for normalization, equation (12) is similar to equation (10). Equation (12) has not been implemented for the eight-axis arm because predetermined information is required on the obstacles in the work space. In unstructured environments

such as space, this method is too limiting because it is not adaptive to unknown obstacles. Other authors have proposed more robust and adaptive methods for obstacle avoidance with redundant manipulators. For instance, Karlen et al. (ref. 18) discuss an algorithm for reflexive obstacle avoidance using proximity sensors along the redundant manipulator. In reference 4, Nenchev presents 21 references dealing in part with obstacle avoidance.

4. Results

The data reported in this section were obtained via graphical simulation. The ARMII manipulator was used for the examples in this section to verify the simulated results on actual hardware.

4.1. Local Optimization Results

This section presents local redundancy optimization results for the full solution. Results are given for joint limit avoidance, manipulability maximization, and a combination of the two. The units are meters per second and radians per second for Cartesian translational and rotational velocities, respectively, and degrees for joint angle. The joint limit constraint function H_J is dimensionless, and the units for manipulability H_M are square meters.

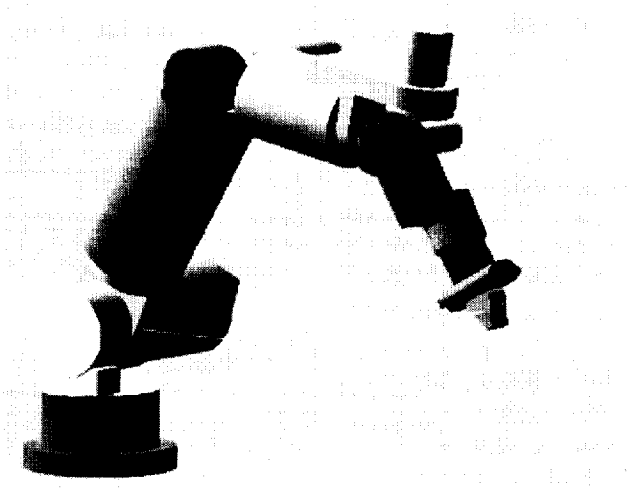

Figure 5. Initial configuration for joint limit avoidance.

4.1.1. Joint limit avoidance. The constraint function used is equation (10) with $n = 8$. The trajectory is an end-effector roll, $\dot{\mathbf{X}} = \{0, 0, 0, 0, 0, 0.4\}^T$. As shown in figure 5, $\boldsymbol{\theta} = \{0, -30, 0, -70, 0, 0, -50, 0\}^T$ is the starting configuration. Table A2 gives the joint limits for the ARMII. Joint 8 was designed to provide continuous bidirectional roll, but the limits were set to $\pm 300°$. The trajectory for this example is satisfied

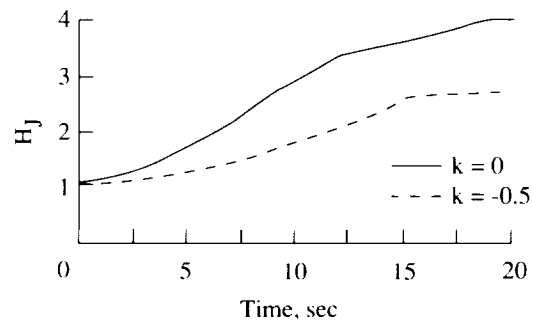

(a) Constraint function.

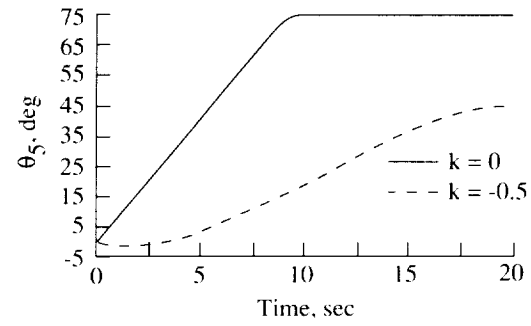

(b) θ_5.

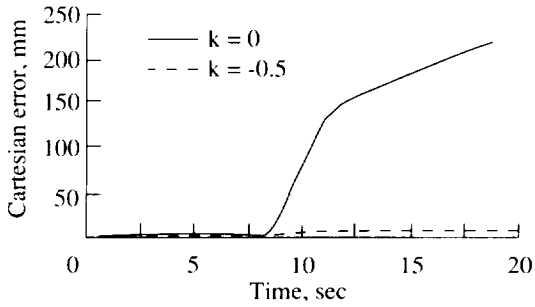

(c) Cartesian error.

Figure 6. Joint limit avoidance.

by a combination of all joints. Figure 6(a) shows the constraint function value for the particular solution only ($k = 0$ in eq. (4b)) and the particular solution with joint limit avoidance (minimization, $k = -0.5$). With no optimization ($k = 0$), the objective function is greater, which means the joints are generally farther from their center of travel and thus nearer to limits. Optimization ($k = -0.5$) improves this situation and forces the joints to be farther from their limits.

A compelling demonstration of the benefit of joint limit avoidance optimization shows when a joint limit is encountered. For the same trajectory, figure 6(b)

shows θ_5 hitting a limit at 9.5 sec, but avoiding the limit when the function is minimized. The associated Cartesian error due to the joint limit is shown in figure 6(c). With joint limit avoidance, the resulting Cartesian trajectory is useful for a larger time span.

4.1.2. Manipulability maximization (singularity avoidance). The constraint function H_M is defined following equation (11). The commanded Cartesian trajectory is $\dot{\mathbf{X}} = \{0.01, 0.01, 0.01, 0, 0, 0\}^T$, and the initial manipulator configuration $\boldsymbol{\theta} = \{0, -10, 75, -70, 0, -80, -90, 0\}^T$ (fig. 7) is near both arm and wrist singularities. Figure 8 shows H_M for the particular solution only ($k = 0$) and with manipulability maximization ($k = 1$). Both curves start with manipulability near zero because the initial configuration is nearly singular. As the curve for $k = 0$ shows, the chosen trajectory tends to increase the manipulability gradually even when no maximization is applied. However, the optimized solution increases the manipulability rapidly and then maintains it at a high level during the move. Both curves fall off rapidly as the trajectory drives the manipulator into the work space limit singularity where $\theta_4 = 0°$. Optimization does nothing to improve this situation because no homogeneous term exists for $\dot{\theta}_4$, as explained in section 3.2.2.

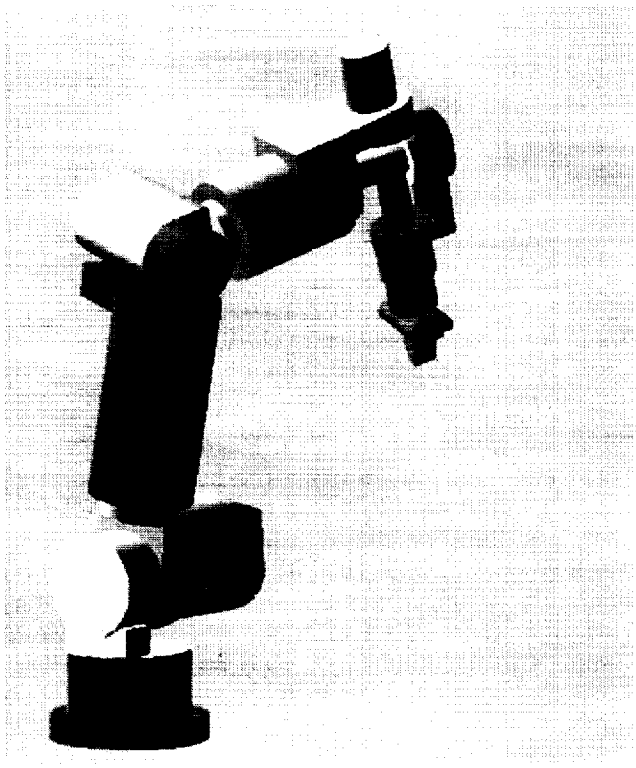

Figure 7. Manipulability maximization for initial configuration.

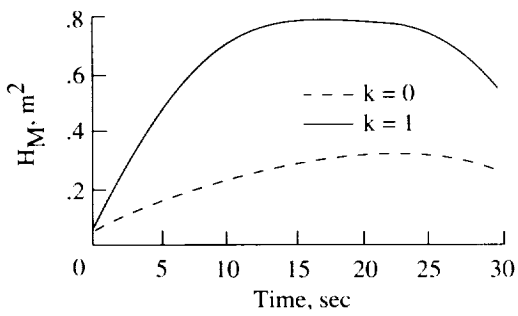

Figure 8. Manipulability maximization for H_M.

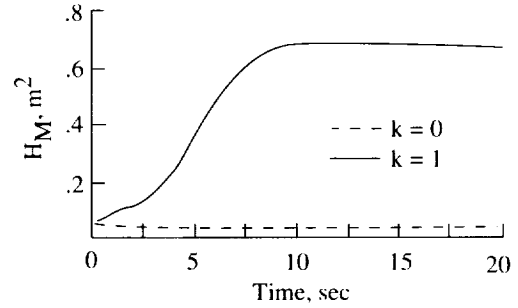

Figure 9. Manipulability maximization for H_M.

Figure 9 dramatically demonstrates the benefits of manipulability maximization. For this figure, the initial manipulator configuration is the same as the one in figure 7, but the Cartesian trajectory is $\dot{\mathbf{X}} = \{0, -0.01, 0, 0, 0, 0\}^T$. Without optimization ($k = 0$), the trajectory drives the manipulator into the neighborhood of the $\theta_6 = -90°$, $\theta_7 = -90°$ internal wrist singularity, and the manipulability measure remains near zero for the entire time. With manipulability maximization ($k = 1$), the manipulator avoids the singularity and achieves the commanded trajectory with high manipulability.

4.1.3. Combined optimization. Experiments with manipulability maximization with the full solution revealed that regions exist where the local maximum for H_M lies outside the joint limits of table A2. The algorithm attempts to increase H_M, but it is not physically realizable because of the physical joint limits. Such cases indicate that combining optimization criteria is sometimes necessary. For the example in this section, the Cartesian command and initial configuration are the same as those for the manipulability example in figure 9. The objective function is constructed to maximize manipulability while avoiding joint limits:

$$H(\boldsymbol{\theta}) = k_M H_M + k_J H_J \qquad (13)$$

where the manipulability and joint limit functions are defined in equations (11) and (10); k_M must be positive to maximize H_M, and k_J must be negative to avoid joint limits.

An example of a case where manipulability maximization and joint limit avoidance must be combined is given in this section. The Cartesian trajectory is $\mathbf{X} = \{0.01, 0.01, 0.01, 0, 0, 0\}^T$. The initial manipulator configuration is $\boldsymbol{\theta} = \{0, -10, 85, -70, 0, -80, -90, 0\}^T$; this configuration is the same as the one in figure 7, with one change: θ_3 starts at 85°, which is 10° closer to the internal arm singularity. In this example, joint limits are reached for θ_7 and θ_3 during the trajectory with manipulability maximization only.

Figure 10(a) compares H_M for manipulability maximization only ($k_M = 1, k_J = 0$) and for manipulability maximization with joint limit avoidance (JLA) ($k_M = 1, k_J = -1$). A third plot shows the manipulability for the trajectory without any optimization, $k = 0$ (actually, $k_M = 0, k_J = 0$) for comparison. Without any optimization ($k = 0$), the manipulability remains low for the entire trajectory. With manipulability maximization and without joint limit avoidance (MM in fig. 10(a)), the manipulability is highest, but this condition is not physically realizable because of the joint limits encountered. A joint limit for θ_7 is reached at 9 sec, which causes the Cartesian error to increase rapidly (fig. 10(b)) as the actual trajectory deviates from the commanded. Because of this error, figure 10(a) shows that without joint limit avoidance, the manipulator reaches the $\theta_4 = 0°$ work space limit singularity (where H_M goes to zero) sooner than it does with joint limit avoidance. With both manipulability maximization and joint limit avoidance (MM + JLA in fig. 10(a)), the manipulability assumes intermediate values that are realizable because no joint limits are encountered. Joint limits were not encountered for the no optimization ($k = 0$) case, and the plot is so similar to MM + JLA in figure 10(b) that it is not included. The instability reflected around 28 sec in figures 10(a) and 10(b) for the MM case is due to the work space limitation singularity; these data were obtained through the use of simulation not the actual ARMII hardware.

4.2. Comparison of Partitioned and Full Solutions

The results presented previously are for the full solution. The partitioned solution is suboptimal because the particular and homogeneous solutions are optimized separately for the translational and rotational parts. However, as shown in the results of this section, the difference is not significant.

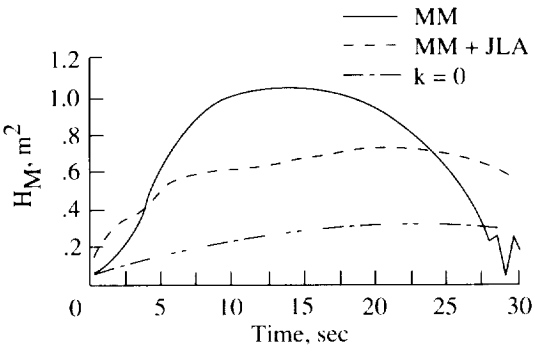

(a) H_M.

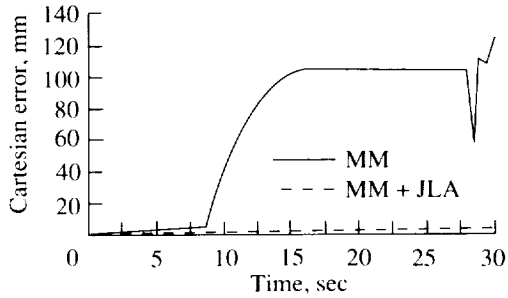

(b) Cartesian error.

Figure 10. Combined optimization.

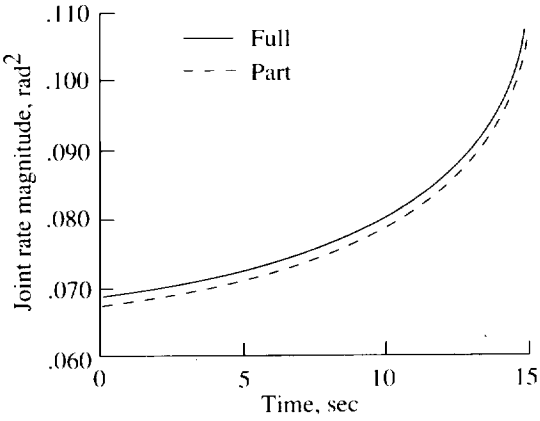

Figure 11. Full vs partitioned joint rate magnitude.

4.2.1. Comparison of particular solutions. The full particular solution (eq. 4(a)) yields the least-squares solution for joint rates. The partitioned particular solutions (eqs. 6(a) and 7(a)) result in a higher Euclidean norm joint rate magnitude. Figure 11 shows a typical result. This simulation moves the manipulator toward the singularity where $\theta_4 = 0°$. The maximum percent difference between the full and partitioned joint rate magnitudes is 2.5, which decreases as the manipulator approaches the singularity.

4.2.2. Joint limit avoidance. The Cartesian trajectory and initial manipulator configuration in this example are $\dot{\mathbf{X}} = \{0, 0, 0, 0, 0, 0.4\}^T$ and $\boldsymbol{\theta} = \{0, -30, 0, -70, 0, 0, -50, 0\}^T$, the same as the example of section 4.1.1. Figure 12 shows joint limit avoidance for the full ($k = -0.5$, repeated from fig. 6(a)) and the partitioned ($k_A = k_W = -0.5$) solutions. The results are nearly identical. The full objective function is only slightly less than the partitioned objective function. Theoretically, the full solution avoids joint limits better than the partitioned because the objective function is minimized to smaller values, but practically there is no difference.

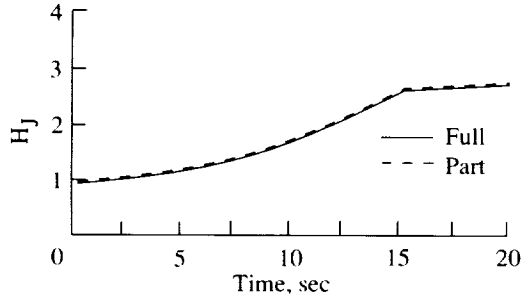

Figure 12. Full vs partitioned joint limit avoidance.

4.2.3. Manipulability maximization. The Cartesian trajectory and initial manipulator configuration in this section are $\dot{\mathbf{X}} = \{0.01, 0.01, 0.01, 0, 0, 0\}^T$ and $\boldsymbol{\theta} = \{0, -10, 75, -70, 0, -80, -90, 0\}^T$, the same as the first example of section 4.1.2. Figure 13 compares manipulabilities for the full ($k = 1$, repeated from fig. 8 with a different vertical scale) and the partitioned ($k_A = k_W = 1$) solutions. The constraint functions for the partitioned case are the arm and wrist manipulabilities, H_A and H_W, defined following equation (11). The units for H_A are m^2 and H_W is dimensionless.

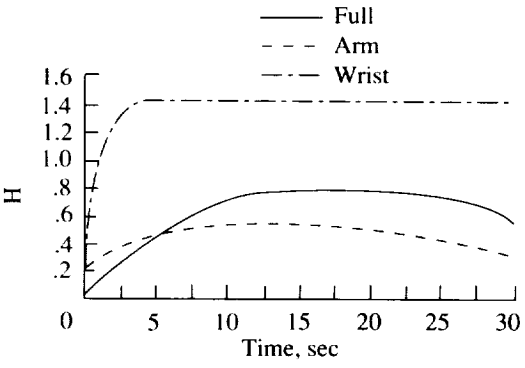

Figure 13. Full vs partitioned manipulability maximization.

Figure 13 shows that the wrist manipulability for the partitioned case increases rapidly to $\sqrt{2}$ and is held there for the remaining trajectory. The partitioned arm manipulability increases to a lower value and falls off as the elbow work space limit singularity is approached. The full manipulability increases to a value in between the arm and wrist curves. It also falls off as the elbow work space limit singularity is approached. Therefore, the wrist manipulability appears to be superior to the full solution, and the arm manipulability tends to be lower than the full solution.

4.2.4. Accuracy of partitioned solution. In the eight-axis singularity analysis of section 3.2.4, the singularities of the partitioned solution were concluded to be identical to those of the full solution; these are the physical manipulator singularities. Therefore, the partitioned solution does not add algorithmic singularities to those found in the full case.

When a determinant is zero, the solution is singular; when it is near zero, the solution is ill-conditioned. The following question arises: Is the partitioned solution ill-conditioned in a larger neighborhood around the singularities than the full solution? To answer this question, joint trajectories were designed to drive the graphical simulation of the manipulator through two work space interior singularities ($\theta_2 = 0°$, $\theta_3 = 90°$ and $\theta_6 = 90°$, $\theta_7 = -90°$) simultaneously, and the full and partitioned $|\mathbf{J}\mathbf{J}^T|$ were studied. Figure 14 shows the manipulator in these singular conditions, where the full configuration is $\boldsymbol{\theta} = \{0, 0, 90, -70, 0, 90, -90, 0\}^T$. This configuration is a combination of those shown in figures 4(a) and 4(c).

Figure 15 presents the results of this study. Starting from $\boldsymbol{\theta} = \{0, -10, 80, -70, 0, 80, -100, 0\}^T$, joints 2, 3, 6, and 7 were updated by 1°/sec, so both singularities were reached at 10 sec. Figure 15 is a plot of $|\mathbf{J}_{5\times7}\mathbf{J}_{5\times7}^T|$ (5×7), $|\mathbf{J}_{1ULA}\mathbf{J}_{1ULA}^T|$ (arm) and $|\mathbf{J}_{LR}\mathbf{J}_{LR}^T|$ (wrist). The arm curve is symmetric; the 5×7 and wrist curves are not because joint 6 hits a limit at the wrist singularity and does not move through.

Figure 15 provides a clear answer to the question of ill-conditioning: The full solution (5×7) is ill-conditioned in a much greater neighborhood around the singularities than the partitioned solutions (arm and wrist). Therefore, the robustness of the partitioned solution is an advantage when compared with the full solution.

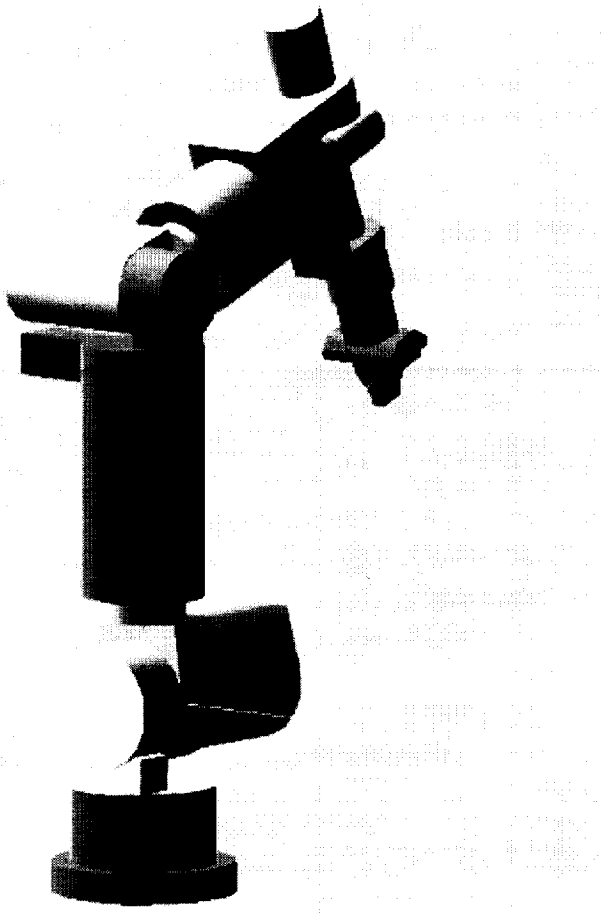

Figure 14. Internal arm and wrist singular configurations.

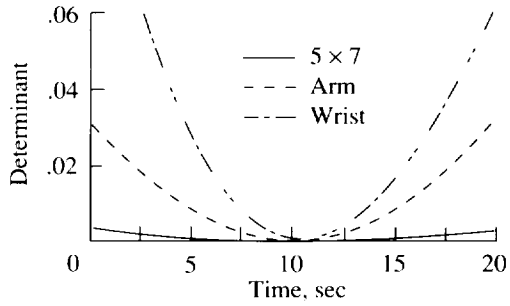

Figure 15. Full vs partitioned solutions near singularities.

5. Eight-Axis Arm Design Limitation

This section discusses a limitation in the eight-axis arm design regarding redundancy optimization. Design alternatives are presented in appendix D to alleviate the problem.

As discussed in section 3.2.1, the length of reach from shoulder to wrist for manipulators with a spherical wrist, spherical shoulder, and a single elbow joint is a function of only the elbow joint angle. Figure 3 shows this relationship. Regardless of the θ_3, θ_5 values, the length SW (fixed by the Cartesian trajectory) is a function of only θ_4. This function is obtained from the cosine law discussed in reference 15. A derivative of this relationship yields the unique solution for $\dot{\theta}_4$ in equation (3).

The limitation in this design is that the elbow joint can only be used to satisfy the primary task, the Cartesian trajectory. As discussed in section 3.2.2, the elbow joint cannot be used in the secondary task of manipulator performance optimization because it does not influence the self-motion of the eight-axis arm. As a trade-off, a benefit of this design is simplified kinematics, and greatly reduced computation requirement when exploiting the independent elbow rate solution and the wrist-partitioned solution.

Although the eight-axis arm has two redundant degrees of freedom, it has only one mode of self-motion, the elbow orbit about the line SW. (See fig. 2.) This self-motion is also achieved by seven-degree-of-freedom manipulators with only one redundant freedom. The question becomes, Is the extra overhead and reduced reliability with the extra joint justified considering only one self-motion mode is achieved and the elbow joint cannot be used for optimization?

Appendix D discusses kinematic design modifications to address the existing eight-axis arm limitations. The emphasis is to provide a second mode of self-motion, in the plane SEW, and to ensure that the elbow joint participates in optimization.

6. Conclusions

This paper presents local redundancy optimization applied to a class of eight-axis redundant arms. The theory has been implemented on a member of the class, the Advanced Research Manipulator II (ARMII). The performance constraints for the secondary task optimization are joint limit avoidance, manipulability maximization (hence singularity avoidance), and a combination of the two. Results are presented to show the effectiveness of the redundancy optimization.

The methods used in this paper are well-known from the redundant manipulator literature. The contributions of this paper are fourfold.

1. Real-time local redundancy optimization for an experimental eight-axis manipulator is demonstrated. Most experimental efforts in the past have used seven-axis arms.

2. A kinematic design limitation of this class of eight-axis arms is explained. The length of reach from the shoulder to the wrist is a function of only the elbow joint angle, which means that the elbow angle participates only in the primary task, and cannot affect the secondary optimization task. Even though there are two redundant degrees of freedom, there is only one mode of self-motion. The geometry is suited for low computation redundancy resolution, but the trade-off is reduced versatility.

3. Symbolic pseudoinverses and objective function gradients are used for both full and partitioned solutions. In addition, for the partitioned solution, the symbolic arm and wrist null-space projection matrices are given.

4. This paper shows that a partitioned solution can be applied to obtain similar optimization results as the full solution, without the introduction of algorithmic singularities. The motivation for the partitioned solution is reduced computation. The partitioned solution is suboptimal because translational and rotational terms are optimized separately for both primary and secondary tasks, but presented results show the difference is not significant. Singularity analysis reveals that no algorithmic singularities exist for the partitioned solution. The partitioned and full solutions share the same physical manipulator singular conditions. Also, the partitioned solution is shown to be ill-conditioned in smaller neighborhoods of the shared singularities than the full solution.

NASA Langley Research Center
Hampton, VA 23681-0001
January 10, 1994

Appendix A

Advanced Research Manipulator II

This appendix describes the Advanced Research Manipulator II (ARMII), which is representative of the class of redundant eight-axis manipulators in figure 1. This appendix also gives the Denavit-Hartenberg parameters and the Jacobian matrix for this class of manipulators.

Figure A1 is a photograph of the ARMII, and figure A2 is a kinematic drawing of the ARMII. The following features distinguish the ARMII from existing industrial manipulators: two redundant degrees of freedom; four-jointed spherical wrist; continuous bidirectional end-effector roll; no kinematic offsets; a high payload-to-weight ratio (1:5); high joint stiffness with 200:1 harmonic gearing at each joint; absolute position potentiometer, input and output relative encoders, temperature sensor, limit switches, and mechanical stops for each joint; high torque direct current brush servomotors with integral brakes and encoders; high link stiffness with graphite or epoxy composite material; and space-flight-qualifiable components.

Table A1. Eight-Axis Arm Denavit-Hartenberg Parameters

i	α_{i-1}	a_{i-1}	d_i	θ_i
1	0	0	0	θ_1
2	90°	0	0	θ_2
3	−90°	0	d_3	θ_3
4	90°	0	0	θ_4
5	−90°	0	d_5	$\theta_5 - 90°$
6	−90°	0	0	$\theta_6 + 90°$
7	90°	0	0	$\theta_7 - 90°$
8	90°	0	0	θ_8

Table A2. ARMII Joint Limits

[Units are in degrees]

i	$\theta_{\max}$	$\theta_{\min}$	θ_{ci}	$\Delta\theta_i$
1	165	−165	0	165
2	90	−90	0	90
3	165	−165	0	165
4	90	−90	0	90
5	75	−255	−90	165
6	90	−90	0	90
7	0	−120	−60	60
8	300	−300	0	300

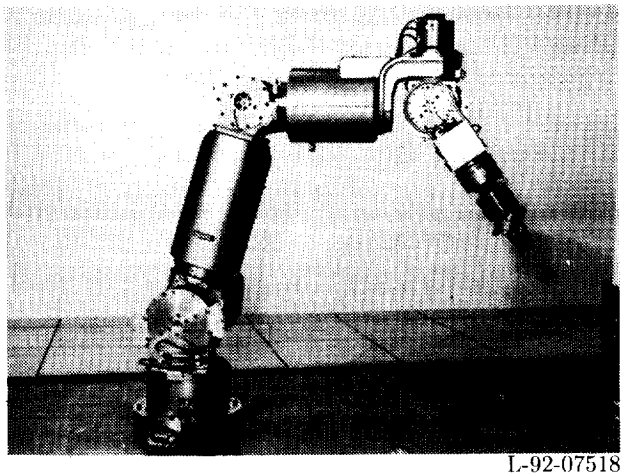

L-92-07518

Figure A1. ARMII photograph.

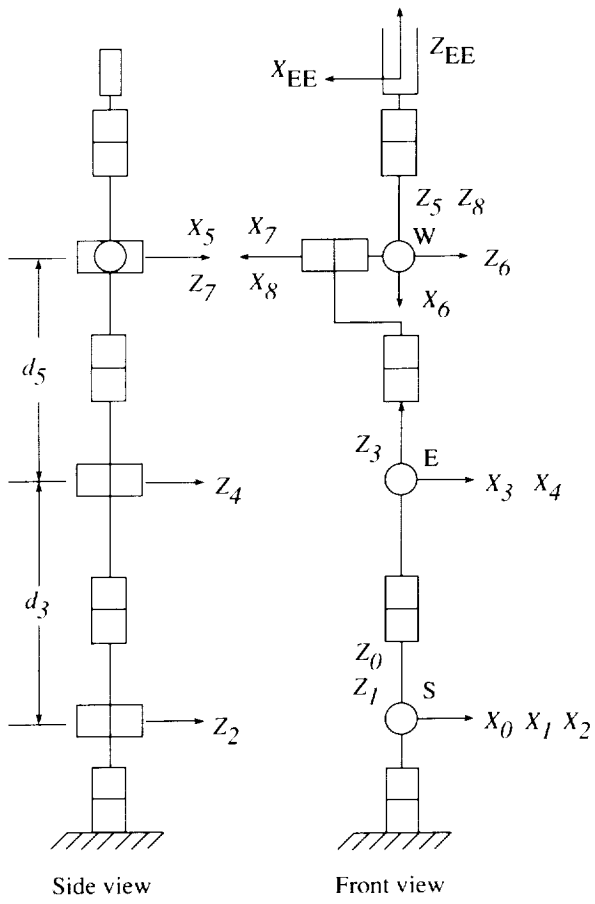

Figure A2. ARMII kinematic diagram.

The eight-axis arm Denavit-Hartenberg parameters (Craig convention (ref. 14)) and ARMII joint limits plus equation (10) terms are given in tables A1 and A2. In table A1, nominal values for the fixed lengths are $d_3 = 695$ mm and $d_5 = 545$ mm.

The Jacobian matrix for the eight-axis arm expressed in the elbow Cartesian coordinate frame, {4}, is presented in reference 13 as follows:

$$ {}^{4}[\mathbf{J}] = \begin{bmatrix} \mathbf{J}_{UL} & 0 \\ \mathbf{J}_{LL} & \mathbf{J}_{LR} \end{bmatrix} $$

$$ \mathbf{J}_{UL} = \begin{bmatrix} -As_2s_3 & -Ac_3 & 0 & -d_5 \\ d_3s_2s_3s_4 & d_3c_3s_4 & 0 & 0 \\ K_{16} & -Bs_3 & d_5s_4 & 0 \end{bmatrix} $$

$$ \mathbf{J}_{LL} = \begin{bmatrix} K_5 & -s_3c_4 & s_4 & 0 \\ -K_6 & s_3s_4 & c_4 & 0 \\ s_2s_3 & c_3 & 0 & 1 \end{bmatrix} $$

$$ \mathbf{J}_{LR} = \begin{bmatrix} 0 & c_5 & s_5c_6 & KK_3 \\ 1 & 0 & -s_6 & c_6c_7 \\ 0 & -s_5 & c_5c_6 & KK_1 \end{bmatrix} $$

where

$$ A = d_3c_4 + d_5 $$

$$ B = d_3 + d_5c_4 $$

$$ K_5 = c_2s_4 + s_2c_3c_4 $$

$$ K_6 = -c_2s_4 + s_2c_3s_4 $$

$$ K_{16} = d_3s_2c_3 + d_5K_5 $$

$$ KK_1 = s_5s_7 + c_5s_6c_7 $$

$$ KK_3 = -c_5s_7 + s_5s_6c_7 $$

Cartesian velocities used with this Jacobian matrix must be expressed in frame {4}. If velocities are commanded in a different frame (e.g., {8}), the following coordinate transformation is required (ref. 13):

$$ {}^{4}\begin{Bmatrix} \mathbf{v} \\ \boldsymbol{\omega} \end{Bmatrix} = \begin{bmatrix} {}^{4}_{8}\mathbf{R} & 0 \\ 0 & {}^{4}_{8}\mathbf{R} \end{bmatrix}^{8} \begin{Bmatrix} \mathbf{v} \\ \boldsymbol{\omega} \end{Bmatrix} $$

Appendix B

Symbolic Partitioned Pseudoinverse

The symbolic form for the pseudoinverse of the partitioned reduced Jacobian matrix is given in this appendix (ref. 15). Because $\dot{\theta}_4$ is solved independently with equation (3), column 4 and row 1 are removed from $\mathbf{J}_{UL}$. Thus, the following translational pseudoinverse, used in equation (7a), is of order 3×2:

$$\mathbf{J}^*_{1ULA} = \frac{1}{D_{UL}} \begin{bmatrix} m_{11} & c_3 K_{11} \\ m_{21} & -s_2 s_3 K_{11} \\ m_{31} & d_5 s_4 \left(1 - c_2^2 s_3^2\right) \end{bmatrix}$$

where

$$D_{UL} = (d_3^2 + d_5^2)s_2^2 + 2d_5 K_7 (d_3 s_2 + d_5 c_2 c_3 s_4)$$

$$m_{11} = \frac{s_3[d_3 K_{12} + d_5^2(s_2 + c_2 c_3 c_4 s_4)]}{d_3 s_4}$$

$$m_{21} = \frac{d_3 s_2 (d_3 s_2 c_3 + d_5 K_{14}) + d_5^2 (s_2^2 c_3 + c_2 s_4 K_{13})}{d_3 s_4}$$

$$m_{31} = \frac{d_5 c_2 s_3 (d_3 c_2 c_3 - d_5 K_8)}{d_3}$$

$$K_7 = s_2 c_4 + c_2 c_3 s_4$$

$$K_8 = s_2 s_4 - c_2 c_3 c_4$$

$$K_9 = 2 s_2 c_4 + c_2 c_3 s_4$$

$$K_{10} = 2 c_2 s_4 + s_2 c_3 c_4$$

$$K_{11} = d_3 s_2 + d_5 K_7$$

$$K_{12} = d_3 s_2 + d_5 K_9$$

$$K_{13} = s_2 c_4 + c_3 K_{10}$$

$$K_{14} = c_2 s_4 + c_3 K_9$$

The 4×3 rotational pseudoinverse used in equation (7b) is as follows:

$$\mathbf{J}^*_{LR} = \frac{1}{D_{LR}} \begin{bmatrix} n_{11} & (2c_6^2 - 1)s_7^2 + 1 & n_{13} \\ n_{21} & c_6 s_7 c_7 & n_{23} \\ n_{31} & -s_6 c_7^2 & n_{33} \\ n_{41} & c_6 c_7 & n_{43} \end{bmatrix}$$

where

$$D_{LR} = 2\left(1 - s_6^2 s_7^2\right)$$

$$n_{11} = c_6 s_7 (c_5 c_7 + 2 s_5 s_6 s_7)$$

$$n_{13} = c_6 s_7 (-s_5 c_7 + 2 c_5 s_6 s_7)$$

$$n_{21} = c_5 K K_7 + 2 s_5 K K_8$$

$$n_{23} = -s_5 K K_7 + 2 c_5 K K_8$$

$$n_{31} = c_6 (2 s_5 + c_5 K K_8)$$

$$n_{33} = c_6 (2 c_5 - s_5 K K_8)$$

$$n_{41} = 2 s_5 s_6 c_7 - c_5 c_6^2 s_7$$

$$n_{43} = 2 c_5 s_6 c_7 + s_5 c_6^2 s_7$$

$$K K_7 = \left(c_6^2 - 2\right)s_7^2 + 2$$

$$K K_8 = s_6 s_7 c_7$$

Appendix C

Symbolic Partitioned Null-Space Projection Matrices

The symbolic null-space projection matrix for $\mathbf{J}_{1UL4}$, which is used in equation (6b), is given as follows. This matrix is symmetric; D_{UL} and K_{11} are given in appendix B.

$$(\mathbf{I}_3 - \mathbf{J}_{1UL4}^{*}\mathbf{J}_{1UL4}) = I_3 - \frac{1}{D_{UL}}\begin{bmatrix} j_{11} & j_{12} & j_{13} \\ & j_{22} & j_{23} \\ & & j_{33} \end{bmatrix}$$

where

$$j_{11} = d_5^2\Big[M_1 - \Big(2s_2^2 - 1\Big)c_3^2 s_4^2\Big] + N_1$$

$$j_{12} = d_5^2 s_2 s_3 c_3 s_4^2$$

$$j_{13} = d_5 K_{11} c_3 s_4$$

$$j_{22} = d_5^2\Big\{M_1 + \Big[2c_3^2 - \Big(c_3^2 + 1\Big)s_2^2\Big]s_4^2\Big\} + N_1$$

$$j_{23} = -d_5 K_{11} s_2 s_3 s_4$$

$$j_{33} = d_5^2\Big(1 - c_2^2 s_3^2\Big)s_4^2$$

$$M_1 = s_2(s_2 + 2c_2 c_3 s_4 c_4)$$

$$N_1 = d_3 s_2(d_3 s_2 + 2d_5 K_7)$$

The symbolic null-space projection matrix for J_{LR}, which is used in equation (7b), is given as follows. This matrix is symmetric; D_{LR} is given in appendix B. The subtraction from the identity matrix is included in the following equation:

$$(\mathbf{I}_4 - \mathbf{J}_{LR}^{*}\mathbf{J}_{LR}) = \frac{1}{D_{LR}}\begin{bmatrix} c_7^2 & -c_6 s_7 c_7 & s_6 c_7^2 & -c_6 c_7 \\ & c_6^2 s_7^2 & -s_6 c_6 s_7 c_7 & c_6^2 s_7 \\ & & s_6^2 c_7^2 & -s_6 c_6 c_7 \\ & & & c_6^2 \end{bmatrix}$$

Appendix D

Kinematic Design Alternatives to the Existing Eight-Axis Manipulator

Kinematic limitations regarding the existing eight-axis arm of figure 1 and their effect on performance optimization using redundancy are discussed in section 5. To provide two modes of self-motion with two redundant joints and to allow the elbow joint to influence performance optimization, kinematic design modifications to the arm of figure 1 are considered in this appendix. Only one change is required: reconfigure joint 5 so that it is parallel to joint 4, as shown in figure D1. With this modification, the subassembly connecting the shoulder to the wrist no longer assembles in only two configurations in plane SEW (elbow up and down) but is a four-bar linkage with one degree of freedom in plane SE_1E_2W. This design has two modes of self-motion: the original elbow orbit (fig. 2), and the new four-bar motion in the plane of the links connecting S and W. These two modes provide more flexibility for obstacle avoidance and null-space optimization than the original design. Since the relationship of equation (3) no longer holds, null-space terms are associated with joint 4.

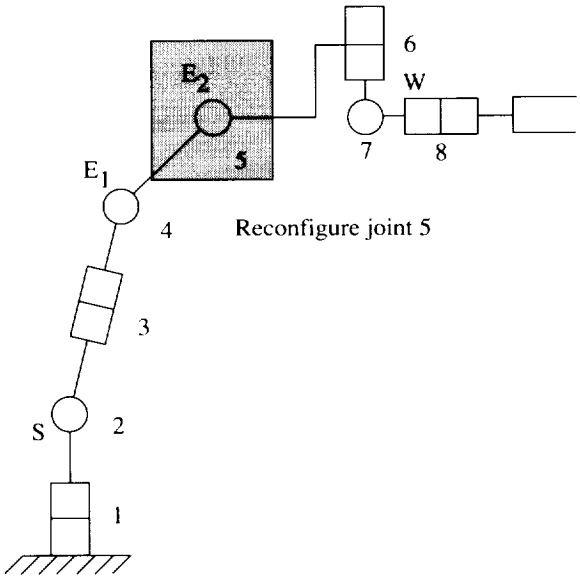

Figure D1. Eight-axis redesign with four-bar self-motion.

An analogous design alternative is to replace the revolute joint 5 with a prismatic joint acting along the line connecting joint 4 and W. (See fig. D2.) In this case, the subassembly connecting S to W is a one-degree-of-freedom slider-crank mechanism with a similar second mode of self-motion in plane SEW.

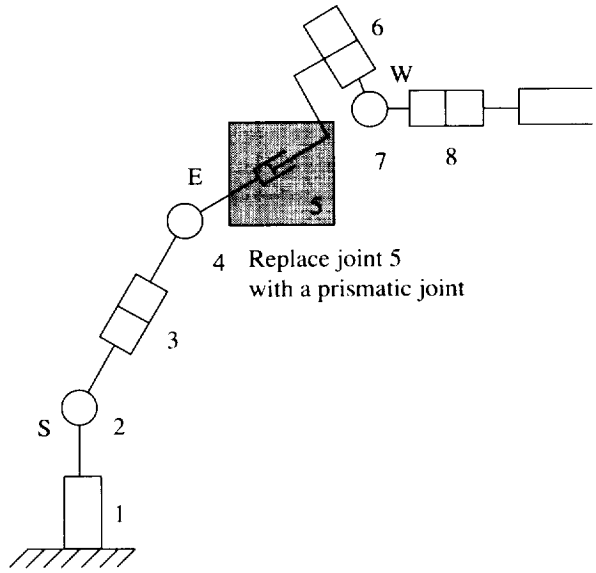

Figure D2. Eight-axis redesign with slider-crank self-motion.

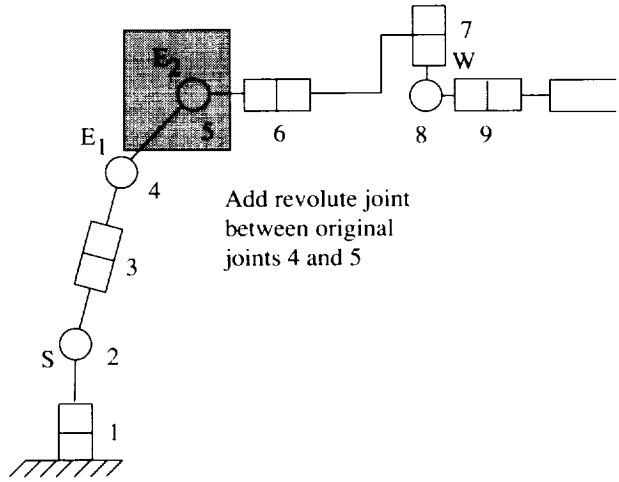

Figure D3. Nine-joint redesign.

A drawback of the proposed design alternatives of figures D1 and D2 is that the four-axis spherical wrist subassembly of the original arm is reduced to three joints. The partitioned solution applied to the new designs would not be useful because the wrist subassembly is no longer redundant, so no wrist performance optimization using self-motion is possible. Therefore, figure D3 proposes a nine-axis redesign where a second elbow revolute joint (parallel to joint 4) is added between joints 4 and 5 of figure 1. (Alternatively, the prismatic joint can be used.) For this concept, there are two self-motion modes, the elbow joint is not excluded from optimization, and a partitioned solution can be applied. However, a similar problem from the original eight-axis arm in

figure 1 exists: there are three redundant degrees of freedom but only two modes of self-motion.

There are trade-offs among the original design of figure 1 and the proposed redesigns of figures D1, D2, and D3. The original design has simpler kinematics, joint 4 variables solved independently, and allows an efficient partitioned solution. However, joint 4 has no null space and only one mode of self-motion. The eight-axis redesign concepts provide two modes of self-motion, a null-space term associated with $\dot{\theta}_4$, but no four-axis spherical wrist to allow a general partitioned solution with reduced computation. The nine-axis redesign provides all desired attributes, at the cost of an extra joint. For general tasks, the nine-axis alternative is recommended by the author, although more work must be done to validate this recommendation.

References

1. Whitney, Daniel E.: Resolved Motion Rate Control of Manipulators and Human Prostheses. *IEEE Trans. Man-Mach. Syst.*, vol. MMS-10, no. 2, June 1969, pp. 47–53.

2. Liegeois, Alain: Automatic Supervisory Control of the Configuration and Behavior of Multibody Mechanisms. *IEEE Trans. Syst., Man, & Cybern.*, vol. SMC-7, no. 12, Dec. 1977, pp. 868–871.

3. Strang, Gilbert: *Linear Algebra and Its Applications*, Third ed. Harcourt Brace Jovanovich, Publ., c.1988.

4. Nenchev, Dragomir N.: Redundancy Resolution Through Local Optimization: A Review. *J. Robot. Syst.*, vol. 6, no. 6, Dec. 1989, pp. 769–798.

5. Klein, Charles A.; and Huang, Ching-Hsiang: Review of Pseudoinverse Control for Use With Kinematically Redundant Manipulators. *IEEE Trans. Syst., Man, & Cybern.*, vol. SMC-13, no. 3, Mar./Apr. 1983, pp. 245–250.

6. Dubey, Rajiv V.; Euler, James A.; and Babcock, Scott M.: Real-Time Implementation of an Optimization Scheme for Seven-Degree-of-Freedom Redundant Manipulators. *IEEE Trans. Robot. & Automat.*, vol. 7, no. 5, Oct. 1991, pp. 579–588.

7. Baillieul, John: Kinematic Programming Alternatives for Redundant Manipulators. *1985 IEEE International Conference on Robotics and Automation*, IEEE Computer Soc. Press, 1985, pp. 722–728.

8. Lee, Sukhan; and Bejczy, A. K.: Redundant Arm Kinematic Control Based on Parameterization. *Proceedings of the 1991 IEEE International Conference on Robotics and Automation*, Volume 1, IEEE Computer Soc. Press, 1991, pp. 458–465.

9. Kirćanski, Manja V.; and Petrović, Tatjana M.: Inverse Kinematic Solution for a 7 dof Robot With Minimal Computational Complexity and Singularity Avoidance. *Proceedings 1991 IEEE International Conference on Robotics and Automation*, Volume 3, IEEE Computer Soc. Press, 1991, pp. 2664–2669.

10. Holt, Kevin: *Inertial-Space Disturbance Rejection for Robotic Manipulators.* NASA CR-191967, 1992.

11. Chevallereau, C.; and Khalil, W.: Efficient Method for the Calculation of the Pseudo Inverse Kinematic Problem. *Proceedings of 1987 IEEE International Conference on Robotics and Automation*, Volume 3, IEEE Computer Soc. Press, 1987, pp. 1842–1848.

12. Podhorodeski, R. P.; Goldenberg, A. A.; and Fenton, R. G.: Resolving Redundant Manipulator Joint Rates and Identifying Special Arm Configurations Using Jacobian Null-Space Bases. *IEEE Trans. Robot. & Automat.*, vol. 7, no. 5, Oct. 1991, pp. 607–618.

13. Williams, Robert L., II: *Kinematic Equations for Control of the Redundant Eight-Degree-of-Freedom Advanced Research Manipulator II.* NASA TM-4377, 1992.

14. Craig, John J.: *Introduction to Robotics—Mechanics and Control*, Second ed. Addison-Wesley Publ. Co., 1989.

15. Williams, R. L., II; and Aldridge, H. A.: Comparison of Pseudoinverse Computation Methods To Control an Eight-Degree-of-Freedom Manipulator. *Proceedings of the Third National Conference on Applied Mechanisms and Robotics*, Volume 2, Nov. 1993, pp. 75-1–75-6.

16. Williams, Robert L., III: *The Double Universal Joint Wrist on a Manipulator: Solution of Inverse Position Kinematics and Singularity Analysis.* NASA TM-104212, 1992.

17. Yoshikawa, Tsuneo: Analysis and Control of Robot Manipulators With Redundancy. *Robotics Research*, M. Brady and R. Paul, eds., MIT Press, 1984, pp. 735–747.

18. Karlen, James P.; Thompson, Jack M., Jr.; Farrell, James D.; and Vold, Havard I.: Reflective Obstacle Avoidance for Kinematically-Redundant Manipulators. *Proceedings of the NASA Conference on Space Telerobotics*, Volume 2, Guillermo Rodriguez and Homayoun Seraji, eds., NASA CR-186857, 1989, pp. 25–37.

REPORT DOCUMENTATION PAGE

Form Approved
OMB No. 0704-0188

1. AGENCY USE ONLY *(Leave blank)*	2. REPORT DATE	3. REPORT TYPE AND DATES COVERED
	March 1994	Technical Paper

4. TITLE AND SUBTITLE
Local Performance Optimization for a Class of Redundant Eight-Degree-of-Freedom Manipulators

5. FUNDING NUMBERS
WU 586-02-11

6. AUTHOR(S)
Robert L. Williams II

7. PERFORMING ORGANIZATION NAME(S) AND ADDRESS(ES)
NASA Langley Research Center
Hampton, VA 23681-0001

8. PERFORMING ORGANIZATION REPORT NUMBER
L-17289

9. SPONSORING/MONITORING AGENCY NAME(S) AND ADDRESS(ES)
National Aeronautics and Space Administration
Washington, DC 20546-0001

10. SPONSORING/MONITORING AGENCY REPORT NUMBER
NASA TP-3417

11. SUPPLEMENTARY NOTES

12a. DISTRIBUTION/AVAILABILITY STATEMENT
Unclassified Unlimited

Subject Category 63

12b. DISTRIBUTION CODE

13. ABSTRACT *(Maximum 200 words)*

Local performance optimization for joint limit avoidance and manipulability maximization (singularity avoidance) is obtained by using the Jacobian matrix pseudoinverse and by projecting the gradient of an objective function into the Jacobian null space. Real-time redundancy optimization control is achieved for an eight-joint redundant manipulator having a three-axis spherical shoulder, a single elbow joint, and a four-axis spherical wrist. Symbolic solutions are used for both full-Jacobian and wrist-partitioned pseudoinverses, partitioned null-space projection matrices, and all objective function gradients. A kinematic limitation of this class of manipulators and the limitation's effect on redundancy resolution are discussed. Results obtained with graphical simulation are presented to demonstrate the effectiveness of local redundant manipulator performance optimization. Actual hardware experiments performed to verify the simulated results are also discussed. A major result is that the partitioned solution is desirable because of low computation requirements. The partitioned solution is suboptimal compared with the full solution because translational and rotational terms are optimized separately; however, the results show that the difference is not significant. Singularity analysis reveals that no algorithmic singularities exist for the partitioned solution. The partitioned and full solutions share the same physical manipulator singular conditions. When compared with the full solution, the partitioned solution is shown to be ill-conditioned in smaller neighborhoods of the shared singularities.

14. SUBJECT TERMS
Manipulator; Redundancy; Eight degrees of freedom; Partitioned solution; Null-space optimization; Pseudoinverse

15. NUMBER OF PAGES
22

16. PRICE CODE
A03

17. SECURITY CLASSIFICATION OF REPORT	18. SECURITY CLASSIFICATION OF THIS PAGE	19. SECURITY CLASSIFICATION OF ABSTRACT	20. LIMITATION OF ABSTRACT
Unclassified	Unclassified		